2009

Performance of a Fire-and-Forget Anti-Tank Missile with a Damaged Wing

John Harris
University of Alabama - Huntsville

Nathan Slegers
George Fox University, nslegers@georgefox.edu

Performance of a fire-and-forget anti-tank missile with a damaged wing

John Harris [a,b], Nathan Slegers [b,*]

[a] *Science Application International Corporation, Huntsville, Alabama, 35805, United States*

[b] *Mechanical and Aerospace Engineering Department, University of Alabama in Huntsville, Huntsville, AL, 35899, United States*

ARTICLE INFO

Keywords:
Missile dynamics
Damage
Missile guidance

ABSTRACT

A mathematical model is developed for an anti-tank missile and its guidance algorithms. The aerodynamic model is separated into two parts, the airframe and external lifting surfaces in order to model damage to the airframe. Radar data is compared to that of the proposed model and it is shown that the model accurately replicates the true flight dynamics. Two types of field handling damage are modeled, a damaged mid-body wing with 50% of its planform area missing, and an un-deployed mid-body wing. Monte Carlo simulations are performed for each type of damage and the eight possible mid-body wing locations. The results predict that the anti-tank guided missile's performance in response to damage is extremely sensitive to the radial location of damage. Vertical mid-body wing damage had little effect on performance while damage to horizontal and adjacent mid-body wings resulted in significant failures. The failure mode demonstrated was not a large increase in impact errors, but rather failure of the seeker used for guidance due to excessive roll and yawing of the airframe.

1. Introduction

Anti-tank guided missile (ATGM) systems are primarily designed to hit and destroy heavily-armored tanks and other armored fighting vehicles. ATGM systems range in size and include shoulder-launched weapons which can be transported by a single soldier, larger tripod mounted weapons which require a squad or team to transport and fire, and vehicle mounted missile systems. The introduction of man-portable ATGM systems with large warheads into the modern battlefield has given infantry the ability to defeat heavily-armored battle tanks at great ranges. First generation man-portable ATGM systems were either manually or semi-autonomously controlled. Manual ATGM systems required input from an operator to steer the missile to the target. Semi-autonomous ATGM systems required the operator to keep the sights on the target until impact while guidance commands were sent to the missile through wires, radio, or laser markings. Modern man-portable ATGM systems such as the Javelin use a thermal seeker at the front of the missile for guidance. Once the target is identified the missile needs no further operator input during flight and is fire-and-forget. A fire-and-forget system provides the operators, the ability to retreat after firing, reducing their vulnerability. One of the great selling points of man-portable systems is the ability of infantry to quickly relocate their position giving them advantages in urban fighting. However, portable ATGM systems can be transported many times over a variety of missions increasing susceptibility to damage. Field handling damage is often not identified until after firing. By their nature, fire-and-forget ATGM systems use precision sensors and guidance; therefore, damage to the ATGM airframe or control surfaces may significantly alter their performance.

Battle damage and its effects have previously been investigated for many systems. Render et al. [1] experimentally investigated projectile damage to airfoils and demonstrated that circular holes were sufficient to represent more realistic

* Corresponding author.
E-mail address: slegers@mae.uah.edu (N. Slegers).

Nomenclature

C_{Di}, C_{Li}	Coefficient of drag and lift for the ith lifting surface
CG	Center of gravity
C_{D0}, C_{D2}	Lifting surface zero lift and parabolic drag coefficient
$C_{L\alpha}$	Lifting surface lift curve slope
C_{LP}, C_{MQ}	Missile body roll and pitch damping coefficient
C_{NA}	Missile body normal force coefficient
C_{X0}, C_{X2}	Missile body zero lift and parabolic axial coefficient
D	Missile diameter
D_T	Distance to target
g	Acceleration due to gravity
I	Missile inertial matrix
I_{xx}, I_{yy}, I_{zz}	Moments of inertia components
K_{PR}, K_{IR}, K_{DR}	Proportional, integral, and derivative roll error gains
K_{PP}, K_{IP}, K_{DP}	Proportional, integral, and derivative pitch error gains
K_{PY}, K_{IY}, K_{DY}	Proportional, integral, and derivative yaw error gains
m	Mass of the missile
p, q, r	Angular velocity components in the body reference frame
$\vec{r}_{LOS}$	Missile to target line-of-sight vector
r_{xi}, r_{yi}, r_{zi}	Vector components of the distance from the airframe CG to the ith lifting surface aerodynamic center.
$S^B_{\vec{r}_A}$	Cross product operator for distance from the CG to the airframe aerodynamic center.
$S^B_{\vec{r}_i}$	Cross product operator for distance from CG to the ith lifting surface aerodynamic center.
$S^B_{\vec{r}_{TVC}}$	Cross product operator for distance from the CG to the thrust vector tab.
T_i	Transformation from missile body to the ith wing frame
T_R	Total missile thrust
V	Missile total velocity
$\vec{V}_i$	Velocity vector of fin or wing in the fin or wing reference frame
x, y, z	Inertial positions of the missile center of gravity
u, v, w	Velocity components of the missile CG
u_i, v_i, w_i	Velocity components of the ith lifting surface in the ith wing reference frame
α_i	The ith lifting surface angle of attack
ϕ_i, γ_i, δ_i	The ith lifting surface roll, sweep, and deflection angle
ρ	Air density
ϕ, θ, ψ	Euler roll, pitch and yaw angles

star patterns in analysis. Hinrichsen et al. [2] investigated missile impact on aircraft structures by considering both body-to-body impact and hydrodynamic effects. It is well known that damaged projectiles with mass and aerodynamic asymmetries can experience a phenomenon called spin-yaw lock-in [3,4]. Mikhail [5] specifically investigated the effects of fin damage on anti-tank kinetic energy projectiles, quantified how it could cause such lock-in effects, and computed flight histories. Identification and estimation of battle damage have also been carried out on different types of systems. Ganguli et al. [6] formulated a method for detecting rotor-system damage from changes in rotor tip response and hub moment vibrations. Similarly Oberholster and Heyns [7] used neural networks to identify axial-flow fan blade damage from vibration and strain signals. Small unmanned vehicle damage has also been investigated by Shore and Bodson [8] who used recursive parameter estimation for fault detection from damage. They incorporated the identified damage information into a reconfigurable control system and demonstrated its utility in flight tests. Later Slegers and Costello [9] developed a variable structure observer to identify control surface damage on a small unmanned system and demonstrated its ability to improve tracking performance. In applications such as manned aircraft, where the systems are not one-time use, it is desirable for the system to respond to battle damage to improve safety and reliability. Recently neural networks, adaptive control, and reconfigurable techniques have been considered in adapting to flight damage [10–13].

The work reported here develops a six degree-of-freedom (DOF) model of the Javelin man-portable ATGM. In addition, a guidance algorithm is developed to mimic the attack modes of the actual system. The aerodynamics of the airframe and external lifting surfaces are modeled separately to isolate possible changes from damage and demonstrate their effects in simulation. Radar data of a Javelin ATGM system is used to verify the accuracy of the proposed model and guidance algorithms. The verified model is used to simulate two types of observed damage in deployed systems; a partially damaged wing, and an un-deployed or missing wing. Monte Carlo simulations are used to show that under some damage the Javelin ATGM system still performs well, while under more severe damage the chance of failure increases. The Javelin ATGM is roll

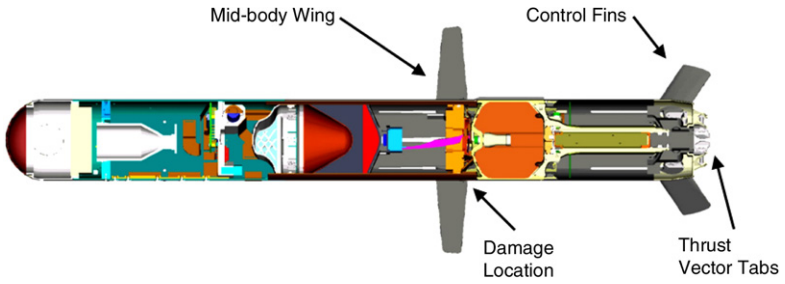

Fig. 1. Javelin missile air frame.

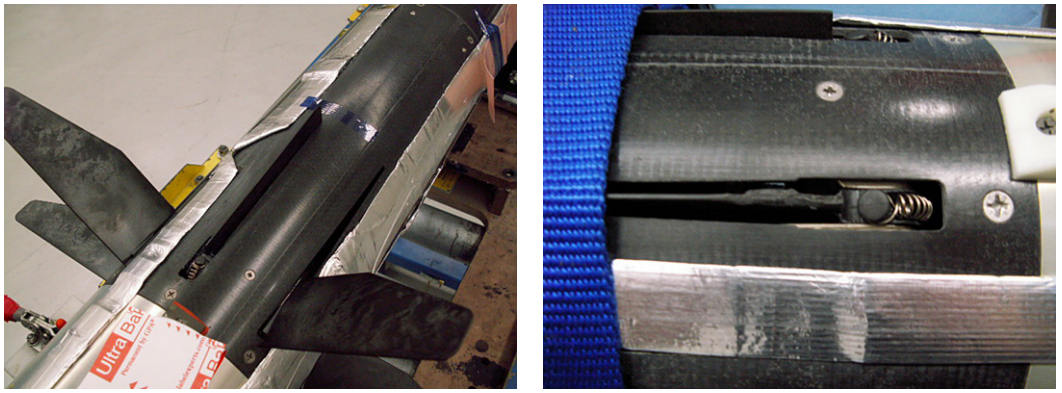

(a) Failure of a mid-body wing to open.

(b) Mid-body wing with root chord damage.

Fig. 2. Field handling damage to mid-body wings.

controlled and it is also demonstrated that the location of the damaged wing around the airframe is a significant factor in its response to damage.

2. Background

The Javelin Weapon System is a man-portable fire-and-forget ATGM system. The system is a two part weapon consisting of a command launch unit (CLU) and a Javelin round. The Javelin round is a missile encapsulated in a carbon fiber launch tube. The launch tube provides environmental protection and electrical interfaces for the missile. The Javelin missile airframe shown in Fig. 1 consists of a five inch diameter body, eight mid-body wings and four rear mounted control fins. Pivot arms are attached to the control fin actuators which operate four thrust vector control tabs. The ogive is an infrared seeker which feeds IR video to the autopilot, thus generating fin commands. The CLU is an infrared sensor used by the operator to detect and identify targets. The missile autopilot is stored in the CLU and loaded to the missile prior to launch. The missile is capable of flying two trajectories; a top attack trajectory and a direct attack trajectory. The trajectory is manually selected by the operator prior to missile activation. However, top attack is the default trajectory and the predominant chosen flight profile.

Javelin began low rate production in 1996 and was fielded in 1997. Operation Iraqi Freedom was the first major deployment of the system and its first true field test. After elimination of armor threats the bulk of the fielded Javelin assets were returned to ammunition depots. The missiles went through a reset process where they were cleaned and evaluated for damage. In the process of evaluating rounds it was discovered that some of the missiles had damaged mid-body wings. The failure review process revealed two failure modes, wings were chipped at the trailing edge of the root chord and wings were failing to open. Representation of wing damage due to field handling drops can be seen below in Fig. 2. As part of the failure review process, drop test were performed to replicate field damage and determine the energy needed to produce said damage. Representation of damage due to drop testing can bee seen in Fig. 3.

Mid-body wings are not used for control of the system, but rather alter the aerodynamics of the airframe. Damage to one or multiple mid-body wings result in asymmetric aerodynamic loads which would not appear on an undamaged system and may lead to excessive yaw, pitch or roll of the airframe. Guidance is based on an infrared seeker requiring the target to remain in the line of sight (LOS) of the seeker. In addition to a LOS view the seeker must have limited roll with respect to the target to maintain a lock with the target. Mid-body wing damage can cause two types of guidance failures. The first occurs when the seeker maintains view of the target but the guidance responds poorly to the damage and misses the target. The second type of failure occurs when excessive yaw, pitch or roll causes seeker failure. This paper uses simulation to predict

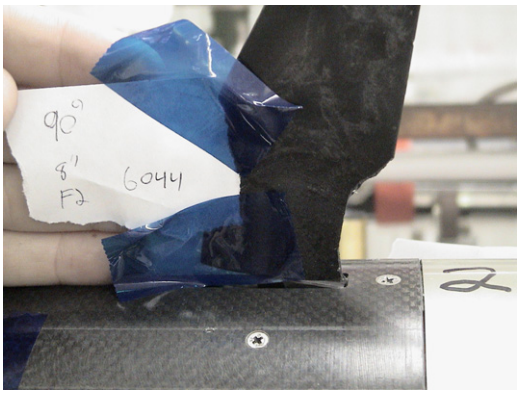

Fig. 3. Test induced root chord damage.

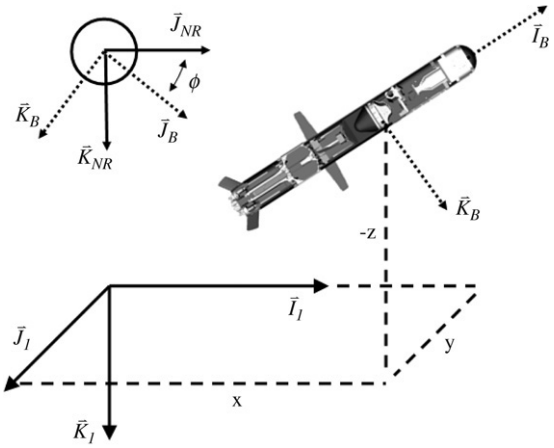

Fig. 4. Coordinate and frame definitions.

the response of a Javelin ATGM to both types of observed mid-body wing damage and estimate the probability of failure in both cases.

3. Anti-tank missile dynamic model

The missile is modeled using six degrees-of-freedom (DOF) which include three inertial positions, x, y, z, and three Euler angles, roll ϕ, pitch θ, and yaw ψ. The missile coordinates are shown in Fig. 4, where the inertial frame is fixed to the earth's surface and the body frame origin is at the missile CG and rotates with the missile. An intermediate non-rolling (NR) frame is fixed to the body but does not roll.

The kinematic differential equations describing the states x, y, z, ϕ, θ, and ψ are provided in Eqs. (1) and (2) where T_{IB} represents the transformation from the inertial to the body reference and the shorthand notation $s_\alpha = \sin(\alpha)$, $c_\alpha = \cos(\alpha)$, and $t_\alpha = \tan(\alpha)$ is used.

$$\begin{Bmatrix} \dot{x} \\ \dot{y} \\ \dot{z} \end{Bmatrix} = [T_{IB}]^{\mathrm{T}} \begin{Bmatrix} u \\ v \\ w \end{Bmatrix} \tag{1}$$

$$\begin{Bmatrix} \dot{\phi} \\ \dot{\theta} \\ \dot{\psi} \end{Bmatrix} = \begin{bmatrix} 1 & s_\phi t_\theta & c_\phi t_\theta \\ 0 & c_\phi & -s_\phi \\ 0 & s_\phi / c_\theta & c_\phi / c_\theta \end{bmatrix} \begin{Bmatrix} p \\ q \\ r \end{Bmatrix} \tag{2}$$

$$T_{IB} = \begin{bmatrix} c_\theta c_\psi & c_\theta s_\psi & -s_\theta \\ s_\phi s_\theta c_\psi - c_\phi s_\psi & s_\phi s_\theta s_\psi + c_\phi c_\psi & s_\phi c_\theta \\ c_\phi s_\theta c_\psi + s_\phi s_\psi & c_\phi s_\theta s_\psi - s_\phi c_\psi & c_\phi c_\theta \end{bmatrix}. \tag{3}$$

The dynamic equations are formed by summing forces and moments about the missile mass center and equating them to the time derivative of linear and angular momentum, respectively. The resulting translation dynamic equations are given

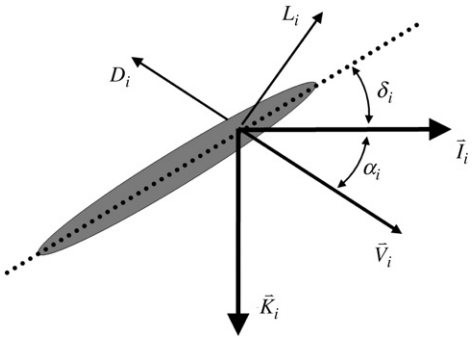

Fig. 5. Wing and reference frame.

in Eq. (4) while the rotational dynamic equations are in Eq. (5).

$$\begin{Bmatrix} \dot{u} \\ \dot{v} \\ \dot{w} \end{Bmatrix} = \begin{bmatrix} 0 & r & -q \\ -r & 0 & p \\ q & -p & 0 \end{bmatrix} \begin{Bmatrix} u \\ v \\ w \end{Bmatrix} + \begin{bmatrix} X/m \\ Y/m \\ Z/m \end{bmatrix} \tag{4}$$

$$\begin{Bmatrix} \dot{p} \\ \dot{q} \\ \dot{r} \end{Bmatrix} = [I]^{-1} \left(\begin{Bmatrix} L \\ M \\ N \end{Bmatrix} + \begin{bmatrix} 0 & r & -q \\ -r & 0 & p \\ q & -p & 0 \end{bmatrix} [I] \begin{Bmatrix} p \\ q \\ r \end{Bmatrix} \right). \tag{5}$$

Components of forces and moments appearing in Eqs. (4) and (5) are expressed in the body reference frame as shown in Eqs. (6) and (7).

$$\mathbf{F} = X\vec{I}_B + Y\vec{J}_B + Z\vec{K}_B \tag{6}$$

$$\mathbf{M} = L\vec{I}_B + M\vec{J}_B + N\vec{K}_B. \tag{7}$$

Forces acting on the missile include contributions from weight, steady aerodynamic forces, wing forces, and thrust vectoring forces.

$$\begin{Bmatrix} X \\ Y \\ Z \end{Bmatrix} = \begin{Bmatrix} X_G \\ Y_G \\ Z_G \end{Bmatrix} + \begin{Bmatrix} X_A \\ Y_A \\ Z_A \end{Bmatrix} + \begin{Bmatrix} X_W \\ Y_W \\ Z_W \end{Bmatrix} + \begin{Bmatrix} X_{TVC} \\ Y_{TVC} \\ Z_{TVC} \end{Bmatrix}. \tag{8}$$

Eq. (9) expresses the missile weight in the body reference frame. For slowly rolling fin stabilized missiles, Magnus forces and moments are typically small and have been neglected. The steady aerodynamic forces of the missile excluding the mid-body wings and fins is defined in Eq. (10).

$$\begin{Bmatrix} X_G \\ Y_G \\ Z_G \end{Bmatrix} = mg \begin{Bmatrix} -s_\theta \\ s_\phi c_\theta \\ c_\phi c_\theta \end{Bmatrix} \tag{9}$$

$$\begin{Bmatrix} X_A \\ Y_A \\ Z_A \end{Bmatrix} = -\frac{\pi}{8} \rho V^2 D^2 \begin{Bmatrix} C_{X0} + C_{X2} \left(v^2 + w^2 \right) / V^2 \\ C_{NA} \left(v/V \right) \\ C_{NA} \left(w/V \right) \end{Bmatrix}. \tag{10}$$

Mid-body wing and fin forces act as point forces at the aerodynamic center of each lifting surface. The orientation of each lifting surface is defined by a sequence of three body-fixed rotations. Starting from the body reference frame the ith lifting surface is successively rotated about $\vec{I}_B$ by the roll ϕ_i, then about the resulting the $\vec{K}$ axis by the sweep γ_i resulting in the ith wing frame. The transformation from the ith wing frame to the body frame is represented by T_i in Eq. (11). A final rotation about $\vec{J}_i$ by the deflection δ_i results in the final orientation of the lifting surface. The lifting surface and the ith wing reference frame are illustrated in Fig. 5 where L_i and D_i are the lift and drag from the ith lifting surface.

$$T_i = \begin{bmatrix} c_{\gamma_i} & -s_{\gamma_i} & 0 \\ c_{\phi_i} s_{\gamma_i} & c_{\phi_i} c_{\gamma_i} & -s_{\phi_i} \\ s_{\phi_i} s_{\gamma_i} & s_{\phi_i} s_{\gamma_i} & c_{\phi_i} \end{bmatrix}. \tag{11}$$

Lift and drag of the ith lifting surface is a function of the surfaces angle of attack. The angle of attack for the ith lifting surface is the combination of the deflection δ_i and the angle of attack of the ith wing frame as shown in Eq. (12) where u_i, v_i and w_i are velocities of the ith lifting surface expressed in the ith wing frame, r_{xi}, r_{yi}, and r_{zi} are the vector components of the

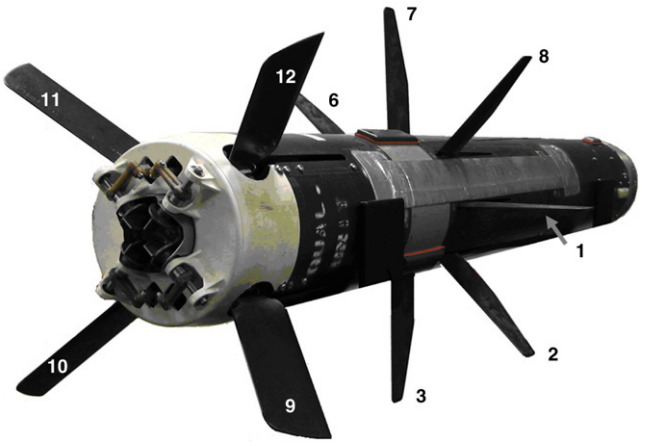

Fig. 6. Control surface definitions.

distance from the airframe CG to the ith lifting surface aerodynamic center, and V_i is the magnitude of the ith lifting surface velocity vector.

$$\alpha_i = \delta_i + \tan^{-1}\left(\frac{w_i}{u_i}\right) \tag{12}$$

$$\begin{Bmatrix} u_i \\ v_i \\ w_i \end{Bmatrix} = [T_i]^{\mathrm{T}} \left[\begin{Bmatrix} u \\ v \\ w \end{Bmatrix} + \begin{bmatrix} 0 & -r & q \\ r & 0 & -p \\ -q & p & 0 \end{bmatrix} \begin{Bmatrix} r_{xi} \\ r_{yi} \\ r_{zi} \end{Bmatrix} \right]. \tag{13}$$

The aerodynamic forces generated by the ith lifting surface with components expressed in the body reference frame are provided in Eq. (14).

$$\begin{Bmatrix} X_i \\ Y_i \\ Z_i \end{Bmatrix} = \frac{1}{2}\rho V_i^2 \, [T_i] \begin{Bmatrix} C_{L_i} \sin(\alpha_i - \delta_i) - C_{D_i} \cos(\alpha_i - \delta_i) \\ 0 \\ -C_{L_i} \cos(\alpha_i - \delta_i) + C_{D_i} \sin(\alpha_i - \delta_i) \end{Bmatrix} \tag{14}$$

$$C_{L_i} = \alpha_i C_{L\alpha} \tag{15}$$

$$C_{D_i} = C_{D0} + C_{D2}\alpha_i^2. \tag{16}$$

The total aerodynamic forces from all eight mid-body wings and four control fins is given by Eq. (17) where the mid-body wings are represented by $i = 1$ to 8 and the control fins by $i = 9$ to 12. Fig. 6 shows the location of each lifting surface. The first mid-body wing, lifting surface 1, is horizontal with $\phi_i = 0$ and no sweep. Each sequential mid-body fin is rotated by $\pi/8$ rad with respect to the previous. Control fins 9–12 have $\phi_i = \pi/4, 3\pi/4, 5\pi/4$, and $7\pi/4$ all having a sweep γ_i of $\pi/6$.

$$\begin{Bmatrix} X_W \\ Y_W \\ Z_W \end{Bmatrix} = \sum_{i=1}^{12} \begin{Bmatrix} X_i \\ Y_i \\ Z_i \end{Bmatrix}. \tag{17}$$

The four Javelin control fins have individual actuators. When exercised, the actuator moves the control fin as well as a thrust vector tab which is connected to the control fin actuators via a pivot arm. The thrust vector tab diverts a quarter of the thrust in the direction of the tab. The TVC tabs have the same roll orientation with respect to the body as fins 9 through 12 but no sweep. Eq. (18) defines the total TVC force in the body frame, where T_R is the total thrust.

$$\begin{Bmatrix} X_{TVC} \\ Y_{TVC} \\ Z_{TVC} \end{Bmatrix} = \frac{1}{4}\sum_{i=9}^{12} T_R \begin{Bmatrix} c_{\delta_i} \\ s_{\phi_i} s_{\delta_i} \\ -c_{\phi_i} s_{\delta_i} \end{Bmatrix}. \tag{18}$$

Moments acting on the missile in Eq. (5) include contributions from the steady aerodynamic, wing, and thrust vector forces and unsteady aerodynamic moments. The convention is used where the vector cross product of two vectors $\vec{r} = \begin{Bmatrix} r_x & r_y & r_z \end{Bmatrix}^{\mathrm{T}}$ and $\vec{F} = \begin{Bmatrix} F_x & F_y & F_z \end{Bmatrix}^{\mathrm{T}}$ both expressed in the A reference frame can be written as in Eq. (20).

$$\begin{Bmatrix} L \\ M \\ N \end{Bmatrix} = \begin{Bmatrix} L_A \\ M_A \\ N_A \end{Bmatrix} + \begin{Bmatrix} L_W \\ M_W \\ N_W \end{Bmatrix} + \begin{Bmatrix} L_{TVC} \\ M_{TVC} \\ N_{TVC} \end{Bmatrix} + \begin{Bmatrix} L_{UA} \\ M_{UA} \\ N_{UA} \end{Bmatrix} \tag{19}$$

Table 1

Javelin mass properties.

Time (s)	Thrust (N)	Mass (kg)	CG (m)	I_{XX} (kg m/s^2)	I_{YY}, I_{ZZ} (kg m/s^2)
0.0	0.0	11.25	0.565	0.0252	0.985
0.3	570	11.16	0.555	0.0250	0.979
0.6	650	11.06	0.544	0.0248	0.973
1.2	750	10.82	0.519	0.0244	0.958
1.8	770	10.58	0.493	0.0239	0.942
2.4	650	10.38	0.471	0.0235	0.929
4.2	50	10.16	0.447	0.0231	0.915
5.2	0.0	10.15	0.446	0.0231	0.914

Table 2
Airframe aerodynamic coefficients excluding wings and fins.

Mach	C_{X0}	C_{X2}	C_{NA}	C_{LP}	C_{MQ}
0.1	0.280	0.477	3.279	−0.042	−1.800
0.3	0.255	0.484	3.298	−0.042	−1.800
0.6	0.242	0.484	3.330	−0.042	−1.800

$$S^A_{\vec{r}}\vec{F} = \begin{bmatrix} 0 & -r_z & r_y \\ r_z & 0 & -r_x \\ -r_y & r_x & 0 \end{bmatrix} \begin{Bmatrix} F_x \\ F_y \\ F_z \end{Bmatrix}. \tag{20}$$

Moments from aerodynamic, wing, and thrust vector forces are provided in Eq. (21) to (22), where the cross product operator $S^B_{\vec{r}_A}$ is for the distance from the mass center to airframe aerodynamic center, $S^B_{\vec{r}_i}$ for the distance from the mass center to the ith lifting surface aerodynamic center, and $S^B_{\vec{r}_{TVCi}}$ for the distance from the mass center to the ith thrust vectoring tab.

$$\begin{Bmatrix} L_A \\ M_A \\ N_A \end{Bmatrix} = S^B_{\vec{r}_A} \begin{Bmatrix} X_A \\ Y_A \\ Z_A \end{Bmatrix} \tag{21}$$

$$\begin{Bmatrix} L_W \\ M_W \\ N_W \end{Bmatrix} = \sum_{i=1}^{12} S^B_{\vec{r}_i} \begin{Bmatrix} X_i \\ Y_i \\ Z_i \end{Bmatrix} \tag{22}$$

$$\begin{Bmatrix} L_{TVC} \\ M_{TVC} \\ N_{TVC} \end{Bmatrix} = \frac{1}{4} \sum_{i=9}^{12} S^B_{\vec{r}_{TVCi}} T_R \begin{Bmatrix} c_{\delta_i} \\ s_{\phi_i} s_{\delta_i} \\ -c_{\phi_i} s_{\delta_i} \end{Bmatrix}. \tag{23}$$

The unsteady aerodynamic moments acting on the missile are provided in Eq. (24).

$$\begin{Bmatrix} L_{UA} \\ M_{UA} \\ N_{UA} \end{Bmatrix} = \frac{\pi}{16} \rho V D^4 \begin{Bmatrix} C_{LP} p \\ C_{MQ} q \\ C_{MQ} r \end{Bmatrix}. \tag{24}$$

The Javelin ATGM is propelled by two propulsion units, the launch motor and flight motor. Initial thrust needed for safe separation from the launch tube is provided by the launch motor. The launch motor is expended before the missile fully leaves the tube creating a soft launch for the operator. After the soft launch, the flight motor provides thrust for 5.2 s propelling the Javelin to its maximum speed. The 6 DOF simulation begins at flight motor ignition with the soft launch modeled with an initial velocity and angular rates. The initial mass of a full rate production Javelin missile excluding launch motor was taken from the Javelin Technical Data Document [14] as 11.25 kg. Moments of inertia for the Javelin missile, excluding the launch motor, are $Ixx = 0.0252$ kg m^2 and both Iyy and $Izz = 0.9847$ kg m^2. Thrust produced by the flight motor is time varying resulting in the total mass, mass center and inertia also to be time varying. Over the 5.2 s flight motor burn, all mass properties and thrust are updated using the values in Table 1.

Aerodynamic coefficients needed for force calculations were generated by missile DATCOM [15]. Three DATCOM models were created to determine the individual contributions of the body, control fins and wings. The first model included only the body and ogive with no lifting surfaces and was used to generate the zero angle-of-attack axial force, parabolic axial force, and normal force coefficients. Control fins were added to a second model. Results were compared to the first model and the difference in the aerodynamic coefficients represents effects from control fins. Fin aerodynamic coefficients were found by equally dividing the effects among each fin. Finally, a complete airframe with both mid-body and wings was evaluated. Differences in the second and third models were evaluated to find the wing aerodynamic coefficients. Table 2 summarizes the aerodynamic coefficients for the airframe excluding wings and fins while Table 3 lists the aerodynamic coefficients of the control fins and mid-body wings with all coefficients defined per radian.

Table 3
Control fin and mid-body wing aerodynamic coefficients.

Coefficient	Value
Mid-body wing	
C_{LA}	1.683
C_{D0}	0.004
C_{D2}	0.268
Control fin	
C_{LA}	0.905
C_{D0}	0.004
C_{D2}	0.111

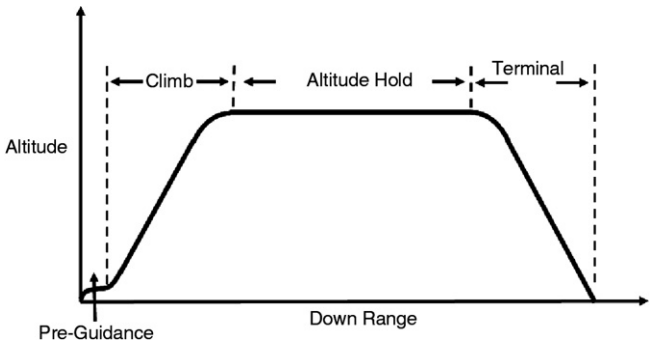

Fig. 7. Javelin trajectory.

4. Control system

Pre-guidance is prior to flight motor ignition. During pre-guidance, the system waits for the ATGM to reach a safe separation distance after firing the launch motor. The 6DOF simulation models pre-guidance by applying initial velocities and Euler Angles. The second phase of flight is climb out. The ATGM climbs at a constant rate until one of two constraints is met, the ATGM reaches an altitude of 120 m, or the line of sight (LOS) of the seeker nears its maximum value. The second condition describes the missile reaching terminal guidance before reaching 120 m and is only met for close range targets. If the altitude reaches 120 m without the LOS reaching its threshold, the missile transitions to altitude hold. As the missile approaches the target in altitude hold mode the seeker angle becomes increasingly negative. Once the seeker angle exceeds its negative limit, the ATGM transitions from altitude hold to terminal guidance. Terminal guidance puts the ATGM on a trajectory for target interception by maintaining a constant seeker angle. Fig. 7 is a visual depiction of the Javelin trajectory previously defined.

Guidance during all stages uses three error signals; roll error (e_R), pitch error (e_P), and yaw error (e_Y). Deflection of the control fins are defined from the proportional–integral–derivative (PID) controller in Eq. (25) where the gain matrices are formed so that a pure roll, pitch and yaw moment are generated from a roll, pitch and yaw error, respectively. Columns one to three of the gain matrices in Eq. (25) perform a pure roll, pitch and yaw maneuver. The sign of each gain in a column is determined by the radial location of control fins 9 to 12. In Fig. 6 it can be seen that a roll is achieved when each control fin has the same deflection, pitch requires control fins 9 and 12 to deflect opposite to that of control fins 10 and 11, and yaw requires fins 11 and 12 to deflect opposite to that of 9 and 10.

$$\begin{Bmatrix}\delta_9\\ \delta_{10}\\ \delta_{11}\\ \delta_{12}\end{Bmatrix}_{NR} = \begin{bmatrix} K_{PR} & -K_{PP} & K_{PY} \\ K_{PR} & K_{PP} & K_{PY} \\ K_{PR} & K_{PP} & -K_{PY} \\ K_{PR} & -K_{PP} & -K_{PY} \end{bmatrix} \begin{Bmatrix} e_R \\ e_P \\ e_Y \end{Bmatrix} + \begin{bmatrix} K_{IR} & -K_{IP} & K_{IY} \\ K_{IR} & K_{IP} & K_{IY} \\ K_{IR} & K_{IP} & -K_{IY} \\ K_{IR} & -K_{IP} & -K_{IY} \end{bmatrix} \begin{Bmatrix} \int e_R \\ \int e_P \\ \int e_Y \end{Bmatrix} + \begin{bmatrix} K_{DR} & -K_{DP} & K_{DY} \\ K_{DR} & K_{DP} & K_{DY} \\ K_{DR} & K_{DP} & -K_{DY} \\ K_{DR} & -K_{DP} & -K_{DY} \end{bmatrix} \begin{Bmatrix} \dot{e}_R \\ \dot{e}_P \\ \dot{e}_Y \end{Bmatrix}. \tag{25}$$

Errors in Eq. (25) are expressed in the body frame. Errors are more conveniently first expressed in the non-rolling frame then transformed to the body frame as shown in Eq. (26).

$$\begin{Bmatrix} e_R \\ e_P \\ e_Y \end{Bmatrix} = \begin{bmatrix} 1 & 0 & 0 \\ 0 & c_\phi & s_\phi \\ 0 & -s_\phi & c_\phi \end{bmatrix} \begin{Bmatrix} e_R \\ e_P \\ e_Y \end{Bmatrix}_{NR}. \tag{26}$$

Prior to terminal guidance the roll, pitch and yaw errors are described in Eq. (27) where it can be seen the desired roll is zero. Pitch and yaw error are generated so that the ATGM will track a desired trajectory defined by y_{DES} and z_{DES} where

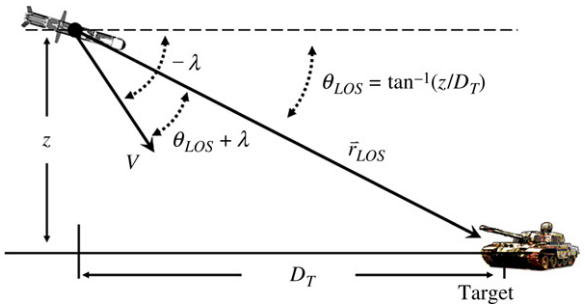

Fig. 8. Glide slope geometry.

Table 4
Controller parameters.

Guidance	K_{PR}	K_{PP} (rad/m)	K_{PY} (rad/m)	K_{IR} (1/s)	K_{IP} (rad/m s)	K_{IY} (rad/m s)	K_{DR} (s)	K_{DP} (rad s/m)	K_{DY} (rad s/m)
Pre-Terminal with TVC	0.100	0.018	0.05	0.0	0.0009	0.0	0.010	0.0033	0.009
Pre-Terminal without TVC	0.200	0.021	0.05	0.0	0.0036	0.0	0.010	0.0060	0.009
Terminal	0.500	37200	0.05	0.0	3100	0.0	0.020	0.0	0.036

the desired altitude is a function of range during climb out and constant during altitude hold.

$$\begin{Bmatrix} e_R \\ e_P \\ e_Y \end{Bmatrix}_{NR} = \begin{Bmatrix} \phi \\ z - z_{DES} \\ y - y_{DES} \end{Bmatrix}. \tag{27}$$

Terminal guidance uses the same roll and yaw errors as pre-terminal guidance. However, pitch error changes as the ATGM achieves target interception by placing itself on a constant glide slope similar to proportional navigation of guided missiles. A diagram of the glide slope guidance is shown in Fig. 8 where r_{LOS} is the line-of-sight vector from the ATGM to the target. As the ATGM approaches the target any misalignment of the velocity vector and r_{LOS} will result in r_{LOS} rotating with the angular velocity ω_{LOS} provided in Eq. (28). Interception with the target will be achieved if the angular velocity of the line-of-sight vector ω_{LOS} is zero. A positive ω_{LOS} signifies the ATGM is falling too fast while a negative ω_{LOS} means it is falling too slowly. Errors during terminal guidance can then be written as in Eq. (29) where ω_{LOS} is multiplied by $\left(D^2/V\right)$ so that both terminal and pre-terminal errors have the same units.

$$\omega_{LOS} = \frac{V}{|\vec{r}_{LOS}|} \sin\left(\theta_{LOS} + \lambda\right) \tag{28}$$

$$\begin{Bmatrix} e_R \\ e_P \\ e_Y \end{Bmatrix}_{NR}^{\text{Terminal}} = \begin{Bmatrix} \phi \\ \omega_{LOS}\left(D^2/V\right) \\ y - y_{DES} \end{Bmatrix}. \tag{29}$$

Control gains appearing in Eq. (25) were selected so that the simplified guidance algorithms in Eq. (25) to (29) model the actual performance of the more complex guidance process. Control gains are provided in Table 4 with each phase of guidance having different values. Increases in pitch gains after TVC occur because of the loss of additional control authority from deflection of exhaust gases during flight motor burn. Pitch gains also dramatically change during terminal guidance due to the use of ω_{LOS} in the pitch error compared to altitude error prior to terminal guidance.

5. Simulation results

The dynamic equations of motion in Eqs. (1)–(5) are highly nonlinear and numerically integrated using a fourth order Runge–Kutta algorithm with a time step of 0.01 s. The missile is fired 1 m above the ground at zero range and cross range with a pitch of 18 deg. The initial velocity after separation is 13 m/s and the roll and pitch rates are −30 and −25 deg/s, respectively. The target is 1985 m down range with terminal guidance initiated when the seeker angle becomes less than −20 deg. To simulate seeker noise during terminal guidance Gaussian random noise with zero mean and standard deviation of 0.17 deg is added to θ_{LOS}. In all cases the maximum control deflection for a surface is 12 deg.

5.1. Undamaged results

The ATGM model and control system developed in Sections 3 and 4 are compared to radar data in Figs. 9–11. It is shown that both the altitude and slant range compare favorably between the model and radar data. The maximum velocity in Fig. 11

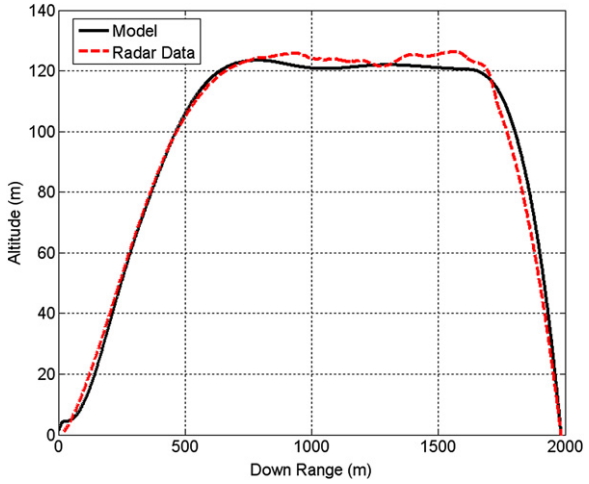

Fig. 9. Down range trajectory comparison.

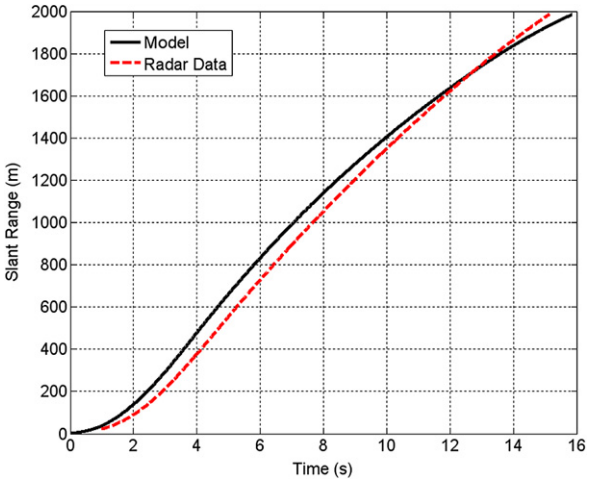

Fig. 10. Slant range comparison.

is similar between the model and radar data, however, the velocity profiles do show a small difference. The minor difference in the velocity profile is expected due to variations in propellant lots and preconditioning of the tactical round.

Figs. 12 and 13 show Euler angles during flight while the angle of attack and control fin deflections are shown in Figs. 14 and 15. Roll and yaw angles in Fig. 13 are small throughout the flight after some initial motion. The pitch is initially large as the ATGM attempts to climb while at an initially low speed. As the speed increases from the launch motor burn the ATGM gradually reduces pitch. A pitch-up moment is achieved by negative deflections of surfaces 9 and 12 along with positive deflections of surfaces 10 and 11. In comparison with the pitch, Figs. 14 and 15 show the initially large control deflections commanded and the resulting angles of attack. Pitch, control deflections, and angle of attack continues to reduce for the next five seconds where altitude hold is reached near the same time as the launch motor burns out. During altitude hold, the speed gradually reduces requiring a gradual increase of pitch and angle of attack. Near 12 s, terminal guidance is reached and control deflections reverse to pitch down the system. As the missile approaches the target, oscillations are observed due to the increasing sensitivity of the seeker angle with respect to change in orientation.

5.1.1. Results with mid-body wing damage

To simulate damaged wings,the planform area of the damaged wing was decreased by 50%. Fifty percent represent the worst case damage reproducible during environmental drops performed by the Close Combat Weapons Systems Project Office and the US Marine Corp [16]. A wing broken at the root chord also results in the wing opening farther than a normally deployed wing. The simulation models this by sweeping the broken wing rearward 45 deg. Simulation of non-deployed or missing wings was achieved by removal of the individual wing forces.

Fig. 16 shows the roll and yaw angles for both damaged and missing mid-body wing 1 according to Fig. 6. Mid-body wing 1 is horizontal and generates lift in normal flight. Reduction or absence of lift from the right side of the airframe creates a roll

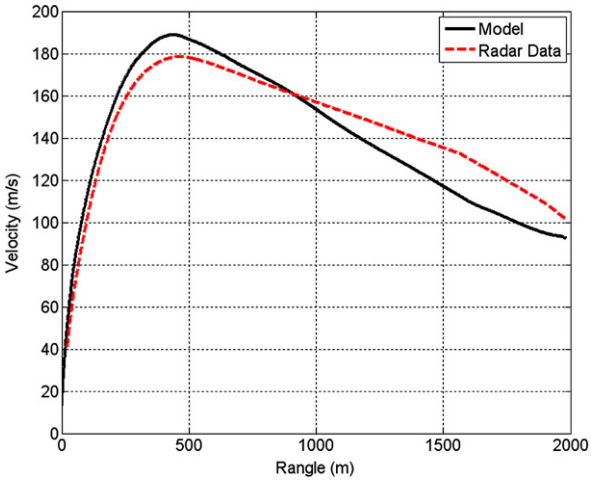

Fig. 11. Down range velocity comparison.

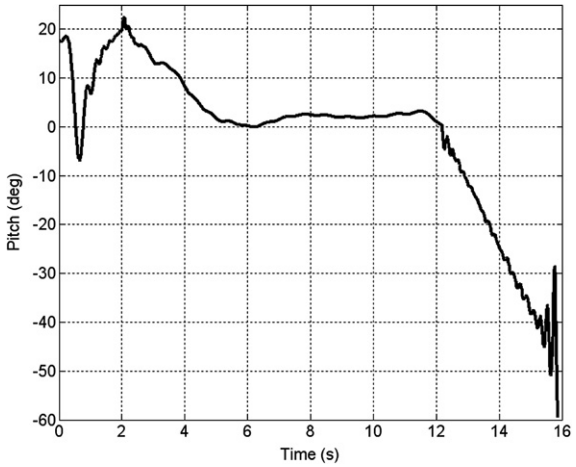

Fig. 12. Euler pitch angle.

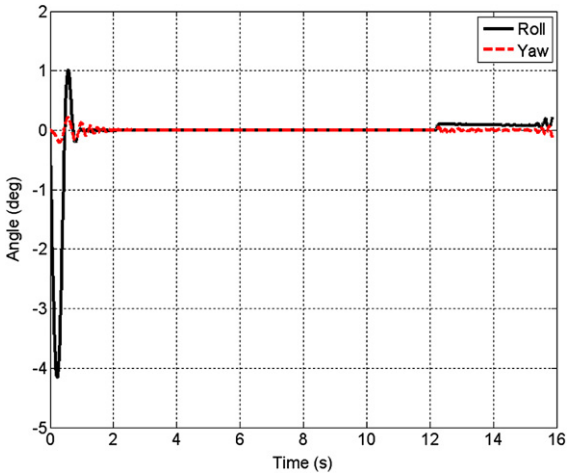

Fig. 13. Roll and yaw angles.

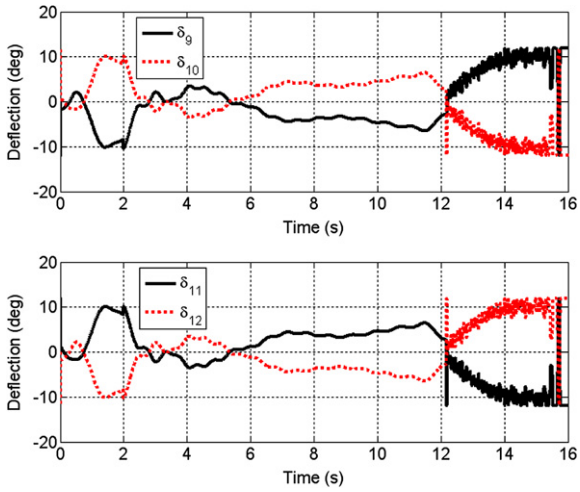

Fig. 14. Fin 1 deflection.

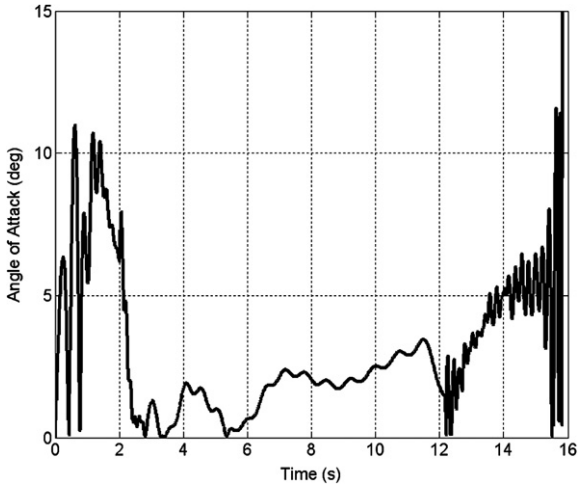

Fig. 15. Angle of attack.

torque that must be compensated by the guidance algorithms. The roll torque produced will be positive when climbing and in altitude hold but negative during terminal guidance. Roll for an undamaged airframe remains small throughout the flight. However, a significant increase in roll is observed during climb and a negative roll during terminal guidance with a mid-body wing is missing. A damaged wing shows similar changes but to less an extent of a missing mid-body wing. Variation in roll from damage also affects yaw. As the airframe rolls, the asymmetry from mid-body wing lift and drag forces results in yawing torque. In addition to asymmetry, saturation of the control fins is significant because in order to cancel large roll torques from damage during terminal guidance, the fins must be differentially canted. If large amounts of deflection are used to roll stabilize the airframe, then less control is available for pitch and yaw control. The effect of both rolling and yawing motion from damage can be seen in the cross range in Fig. 17. During the final seconds of terminal guidance the large asymmetric forces generated result in a final swerve away from the target.

Given the nature of the failure any one of the eight mid-body wings could fail. Therefore all eight wings were altered individually and Monte Carlo simulations were performed. Results for the Monte Carlo simulations are captured in two forms, seeker angle failures, and circular error probable (CEP) defined by the radius which includes the closest 50% of the impacts. Given that the Javelin missile requires the seeker to maintain a LOS lock with the target, it is apparent that large Euler angles can result in failure. In all cases failure of the seeker was assumed to occur when the roll or yaw angle was greater than 20 deg. Tables 5 and 6 report CEP values and Euler angle failure rates for six target locations for both types of damage to each of the eight mid-body wings. The six target locations represent stationary targets at 1000 and 2000 m, and moving targets at 50 m in front and behind the stationary targets. Nominal CEP values with no damage are shown in the right column.

Table 5 shows that for the damaged wing, the CEP only slightly increases except for the 950 m target. For all cases it is the horizontal mid-body wings 1 and 5 which result in the largest CEP values because they generate the largest forces while

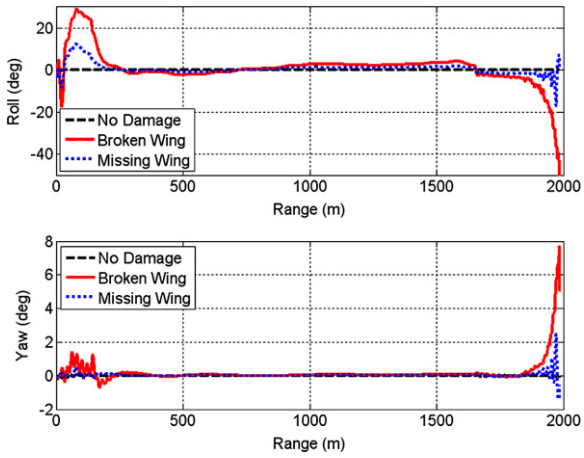

Fig. 16. Roll and pitch from mid-body wing damage.

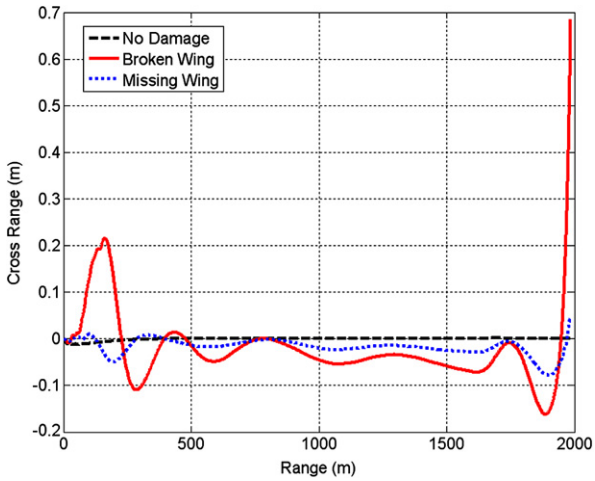

Fig. 17. Cross range from mid-body wing damage.

Table 5
Damaged wing CEP.

Target distance	Wing 1 CEP (m)	Wing 2 CEP (m)	Wing 3 CEP (m)	Wing 4 CEP (m)	Wing 5 CEP (m)	Wing 6 CEP (m)	Wing 7 CEP (m)	Wing 8 CEP (m)	Nominal CEP (m)
2050	0.17/0%	0.15/0%	0.16/0%	0.19/0%	0.16/0%	0.21/0%	0.20/0%	0.17/0%	0.17/0%
2000	0.16/0%	0.22/0%	0.24/0%	0.23/0%	0.16/0%	0.18/0%	0.18/0%	0.19/0%	0.17/0%
1950	0.20/0%	0.21/0%	0.20/0%	0.26/0%	0.16/0%	0.18/0%	0.17/0%	0.18/0%	0.15/0%
1050	0.67/0%	0.53/0%	0.23/0%	0.56/0%	0.69/0%	0.66/0%	0.27/0%	0.64/0%	0.23/0%
1000	0.78/0%	0.61/0%	0.28/0%	0.62/0%	0.81/0%	0.57/0%	0.29/0%	0.55/0%	0.27/0%
950	3.56/88%	3.31/0%	0.25/0%	3.32/0%	3.58/88%	2.80/0%	0.39/0%	2.80/0%	0.28/0%

pitching down in terminal guidance. The largest errors for the damaged airframe occur for the closest target at 950 m. The 950 m target requires the most control to pitch down because the velocity is the highest and the target is moving towards the ATGM. The 950 m CEP values are more than 10 times larger than the nominal case for the horizontal mid-body wings and those adjacent to the horizontal wings, 8, 2, 4, and 6. The seeker failed 88% of the time only for the 950 m target when either of the horizontal mid-body wings was damaged.

Results for a missing wing show a similar trend with respect to mid-body wing orientation. Failure for a missing horizontal wing is the most severe with 100% seeker failure in most cases. Missing mid-body wings next to horizontal wings (8, 2, 4, and 6) have smaller CEP values when compared to horizontal wings but still result in significant failure percentages. Results show missing a vertical mid-body wing, either 3 or 7, results in no seeker failure and CEP values only slightly larger when than an undamaged case.

Table 6
Un-deployed wing CEP.

Target distance	Wing 1 CEP (m)	Wing 2 CEP (m)	Wing 3 CEP (m)	Wing 4 CEP (m)	Wing 5 CEP (m)	Wing 6 CEP (m)	Wing 7 CEP (m)	Wing 8 CEP (m)	Nominal CEP (m)
2050	1.02/100%	0.54/2%	0.17/0%	0.59/4%	1.01/100%	0.32/100%	0.19/0%	0.32/100%	0.17/0%
2000	0.95/100%	0.53/2%	0.17/0%	0.53/4%	0.93/100%	0.37/100%	0.17/0%	0.29/100%	0.17/0%
1950	2.94/100%	1.4/2%	0.17/0%	1.55/4%	2.90/100%	0.31/100%	0.22/0%	0.26/100%	0.15/0%
1050	0.39/0%	0.35/ 0%	0.25/0%	0.30/0%	0.38/0%	0.42/0%	0.28/0%	0.4 /0%	0.23/0%
1000	0.52/20%	0.74/ 0%	0.26/0%	0.74/0%	0.51/15%	0.42/0%	0.23/0%	0.41/0%	0.27/0%
950	1.06/100%	0.83/100%	0.32/0%	0.84/100%	1.04/100%	3.52/100%	0.33/0%	3.52/100%	0.28/0%

6. Conclusion

A mathematical model was developed for a 6 DOF anti-tank missile (ATGM) and its guidance algorithms. In addition, field handling damage was modeled by separation of the missile body and mid-body wings in the aerodynamic model. Radar data from an ATGM was compared to the proposed model and it was shown the model accurately replicated the flight dynamics.

Two types of field handling damage were modeled, a damaged mid-body wing with 50% of its planform area, and an un-deployed or missing mid-body wing. It was shown that asymmetries from damage cause large rolling motion. The rolling motion resulted in high risk of saturation of the control fins and swerving near the end of terminal guidance. Monte Carlo simulations were performed for each type of damage on all eight mid-body wings. Results showed that a damaged wing only slightly altered CEP performance in all cases except a short range target moving toward the ATGM. In the case of a short range target the damage resulted in a large percentage of seeker failure when the horizontal or adjacent mid-body wings were damaged. In all scenarios damage to a vertical mid-body wing had little effect of performance. A missing or un-deployed wing resulted in significant reduction in performance with 100% seeker failure in many cases involving a horizontal and adjacent mid-body wing. However, if the vertical mid-body wing was missing the seeker failure rate was 0% and CEP values were only slightly affected.

Results showed that changes to ATGM performance from observed field damage are extremely sensitive to the location of damage. Vertical mid-body wing damage had little effect on performance while damage to horizontal and adjacent mid-body wings resulted in significant failures. The failure mode demonstrated was not a large increase in CEP but rather seeker failure due to excessive roll and yawing of the airframe. This highlights that the seeker and seeker gimbal performance are significant factors in an ATGM's ability to tolerate field handling damage.

References

[1] P. Render, S. de Silva, A. Walton, M. Mahmoud, Experimental investigation into the aerodynamics of battle damaged airfoils, J Aircr. 44 (2) (2007) 539–549.
[2] R. Hinrichsen, A. Kurtz, J. Wang, C. Belcastro, J. Parks, Modeling projectile damage in transport aircraft wing structures, AIAA J. 46 (2) (2008) 328–335.
[3] D.A. Price, L.E. Ericsson, A new treatment of roll-pitch coupling for ballistic re-entry vehicles, AIAA J. 8 (9) (1970) 1608–1615.
[4] C. Murphy, Some special cases of Spin-Yaw lock-in, J. Guid. Control Dyn. 12 (6) (1989) 771–776.
[5] A. Mikhail, Fin damage and mass offset for kinetic energy projectile spin/pitch lock-in, J. Spacecr. Rockets. 35 (3) (1998) 287–295.
[6] R. Ganguli, I. Chopra, D. Hass, Formulation of a helicopter rotor system damage detection methodology, J. Am. Helicopter Soc. 41 (4) (1996) 302–312.
[7] A.J. Oberholster, P.S. Heyns, On-line fan blade damage detection using neural networks, Mech. Syst. Signal Process 20 (1) (2006) 78–93.
[8] D. Shore, M. Bodson, Flight testing of a reconfigurable control system on an unmanned aircraft, J. Guid. Control Dyn. 28 (4) (2005) 698–707.
[9] N. Slegers, M. Costello, Variable structure observer for control bias on unmanned air vehicles, J. Guid. Control Dyn. 30 (1) (2007) 281–286.
[10] J. Boskovic, R. Mehra, Intelligent adaptive control of a tailless aircraft under wing damage, J. Guid. Control Dyn. 23 (5) (2000) 876–884.
[11] J. Boskovic, R. Prasanth, R. Mehra, Retrofit fault-tolerant flight control design under control effector damage, J. Guid. Control Dyn. 30 (3) (2007) 703–712.
[12] N. Nguyen, K. Krishnakumar, J. Kaneshige, P. Nespeca, Flight dynamics and hybrid adaptive control of damaged aircraft, J. Guid. Control Dyn. 31 (3) (2008) 751–764.
[13] D. Shin, R, Y. Kim, Reconfigurable flight control system design using adaptive neural networks, IEEE Trans. Control. Syst. Technol. 12 (1) (2004) 87–100.
[14] Data Document for the Javelin Antitank Weapons System (U). TI/Martin Javelin Joint Venture, DT-0023 Revision K. Tucson, AZ. 2000.
[15] W. Blake, Missile DATCOM, Wright Patterson Air Force Base, WL-TR-93-3043, Feb. 1998.
[16] D. Lanham, Design and qualification report for the javelin launch tube ruggedization program navel surface warfare center, NSWCCR/RDTR-07/27, Crane, IN, April 2007.